Computers and Structures 268 (2022) 106813

Contents lists available at ScienceDirect

Computers and Structures

journal homepage: www.elsevier.com/locate/compstruc

Additional overlapping finite elements – The pyramid and prism elements

Sungkwon Lee, Klaus-Jürgen Bathe *

Department of Mechanical Engineering, Massachusetts Institute of Technology, Cambridge, MA 02139, USA

ARTICLE INFO

Article history:
Received 7 February 2022
Accepted 26 April 2022
Available online 14 May 2022

Keywords:
Finite elements
Overlapping elements
Pyramid
Prism
Stability and accuracy
AMORE scheme

ABSTRACT

Our objective in this paper is to present two new overlapping finite elements: a pyramid element and a prism element. These elements are useful when meshing general three-dimensional geometries in providing the possibility to transition between other overlapping and traditional elements. Both new overlapping elements are compatible with overlapping brick and tetrahedral elements, and when used as coupling elements also with the traditional finite elements. We theoretically formulate the two new overlapping finite elements, show that only the rigid body modes correspond to zero eigenvalues (hence the elements contain no spurious zero energy mode), show that the patch test is passed, and test the elements for their convergence behavior and condition numbers. We also show that the elements are quite insensitive to element distortions and revisit the imposition of displacement boundary conditions. Finally, we give some illustrative applications using the AMORE scheme in which also the new overlapping elements are employed.

1. Introduction

In finite element analysis, the discretization of complex geometries of the analysis domain often requires the use of geometrically distorted elements. However, element distortions can lead to poor predictive capability of the elements and hence insufficient accuracy of the solution [1,2]. The overlapping finite elements we proposed show great distortion-insensitivity and can be effectively used in the AMORE scheme for "automatic meshing with overlapping and regular elements" [3–8]. In the AMORE scheme, the interior of the analysis domain is first filled with undistorted traditional elements to by-pass the loss of accuracy due to element distortions [1]. The regions that are not filled with the traditional elements are then discretized using overlapping finite elements which exhibit only a small loss of accuracy when distorted. The aim in this judicious use of both the traditional finite elements and overlapping elements is to perform the analysis effectively while expending much less effort on meshing.

We recently proposed an enhanced overlapping finite element scheme [8]. The enhanced formulation enables the efficient calculation of the element stiffness matrices and more importantly provides a positive definite stiffness matrix when used with the polynomial bases considered in Ref. [8]. We recall that the positive definiteness can be absent in other generalized finite element methods based on polynomial enrichments [9,10]. While we gave the details for the enhanced triangular, quadrilateral, tetrahedral, and brick overlapping elements, the same formulation can also be applied to establish other elements.

We want to use the overlapping finite element method effectively for complex geometries of analysis domains and various displacement boundary conditions. Hence in this paper we suggest important further ingredients for the method. First, we introduce a pyramid overlapping element and then a prism overlapping element. These elements allow more flexibility for the AMORE scheme to mesh a complex analysis domain. Furthermore, they are quite effective even when used alone in analyses. Second, we study the use of coupling elements for imposing the Dirichlet (displacement) boundary conditions. This method was already used in our previous paper [4], but in this paper we further show its effectiveness. This technique is particularly useful when a Dirichlet condition is imposed on a *curved* boundary. We have also imposed the displacement boundary conditions by another scheme, namely appropriately defining nodal functions on the boundaries [8]. However, we then found that the strategy of Ref. [8] does not lead to good convergence behavior when the boundary is curved. The use of coupling elements is effective for imposing various displacement boundary conditions since it allows to impose the conditions as in the traditional finite element method [1].

* Corresponding author.
E-mail address: kjb@mit.edu (K.J. Bathe).

https://doi.org/10.1016/j.compstruc.2022.106813
0045-7949/

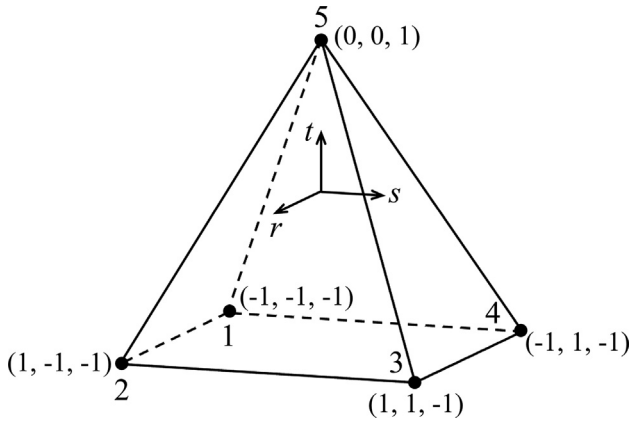

Fig. 1. Reference element used for the geometry interpolation of the pyramid overlapping element.

Table 1
Numerical integration rules used for the pyramid overlapping element; the Gauss quadrature rule is used along each natural coordinate [1]; the number of integration points for the *t*-direction is given with the rules for integrating over the respective plane of the *r*- and *s*-directions, see Fig. 2.

Basis	*t*-direction	*r*- and s-directions
Linear	3	2×2
		3×3
		3×3
Bilinear	4	2×2
		3×3
		3×3
		4×4
Quadratic	4	2×2
		3×3
		4×4
		4×4

In the following section, we first introduce the new pyramid and prism overlapping elements and discuss their stability. Thereafter, we revisit the coupling element formulation and show how the formulation is used for imposing the displacement boundary conditions also on curved boundaries. In Section 3, we provide numerical examples to illustrate the new features of the overlapping element approach. Finally, in Section 4 we provide our concluding remarks.

2. New ingredients for the overlapping finite element method

We present herein the pyramid and prism overlapping elements which are stable and pass the patch test when used with proper numerical integration schemes. The coupling element formulation is revisited, and its effectiveness in prescribing a Dirichlet condition on a curved boundary is described.

2.1. The pyramid overlapping finite element

We use the approach introduced in our previous work [8] to formulate the pyramid overlapping element. A displacement component (e.g., *x*-displacement) is constructed as

$$u(\boldsymbol{x}) = \sum_{I=1}^{5} h_I \psi_I \tag{1}$$

where the h_I are the traditional pyramid element functions [1] and ψ_I is the field of the polyhedral element corresponding to node *I*. The polyhedral element using node *I* is defined to correspond to all elements that share node *I*. The field ψ_I is interpolated as

$$\psi_I = \sum_{K=1}^{5} \phi_K^I \, u_K \tag{2}$$

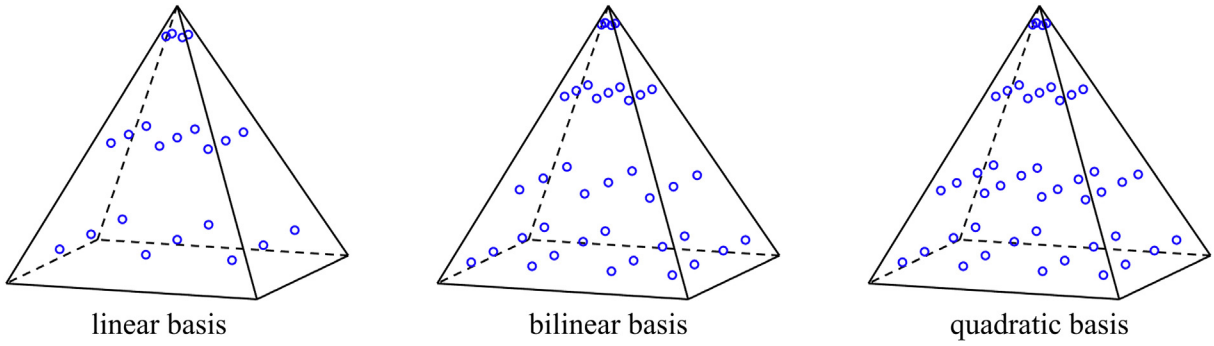

Fig. 2. Locations of the numerical integration points provided in Table 1.

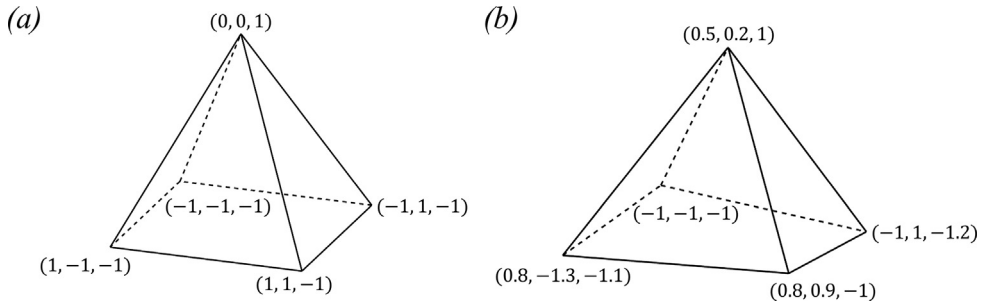

Fig. 3. Pyramid elements used for the zero energy mode test; the Cartesian coordinates (x, y, z) of nodes are given; units in m; (a) Undistorted pyramid element; (b) Distorted pyramid element.

Table 2
Zero energy mode test for the pyramid overlapping elements; the eigenvalues λ_i are given in ascending order; the first, second, and third rows correspond to the use of the linear, bilinear, and quadratic basis, respectively; in all cases, we regard the very small values of $\lambda_1, \lambda_2, \ldots$, and λ_6 as zeros.

element	λ_1	λ_2	λ_3	λ_4	λ_5	λ_6	λ_7	λ_8
Undistorted	-1.55×10^{-7}	-8.86×10^{-8}	-1.47×10^{-8}	8.87×10^{-8}	2.22×10^{-7}	3.41×10^{-7}	6.37×10^{4}	9.91×10^{4}
	-3.58×10^{-7}	-3.86×10^{-8}	-1.90×10^{-8}	6.72×10^{-8}	1.67×10^{-7}	3.62×10^{-7}	3.74×10^{2}	4.74×10^{2}
	-4.07×10^{-7}	-1.85×10^{-7}	-5.70×10^{-8}	4.47×10^{-8}	7.55×10^{-8}	1.54×10^{-7}	7.73×10^{0}	7.73×10^{0}
Distorted	-3.04×10^{-7}	-1.71×10^{-7}	-9.27×10^{-8}	-2.25×10^{-8}	1.23×10^{-8}	3.30×10^{-7}	5.82×10^{4}	6.99×10^{4}
	-2.71×10^{-7}	-2.09×10^{-7}	-7.04×10^{-8}	-1.39×10^{-8}	1.74×10^{-7}	2.04×10^{-7}	4.49×10^{2}	5.96×10^{2}
	-3.37×10^{-7}	-2.03×10^{-7}	-1.21×10^{-7}	-2.77×10^{-8}	1.40×10^{-7}	3.43×10^{-7}	6.52×10^{0}	7.09×10^{0}

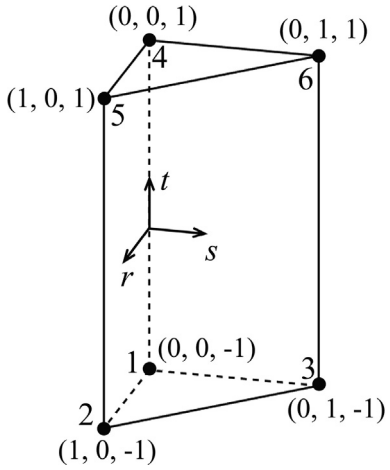

Fig. 4. Reference element for the geometry interpolation of the prism overlapping element.

Table 3
Numerical integration rules used for the prism overlapping element; the rules given in Ref. [11] are used for the integrations over the *r*- and *s*-directions while the Gauss quadrature rule is employed for the *t*-direction integration.

Basis	*r*- and *s*- direction	*t*-direction
Linear	6	3
Bilinear	9	4
Quadratic	12	4

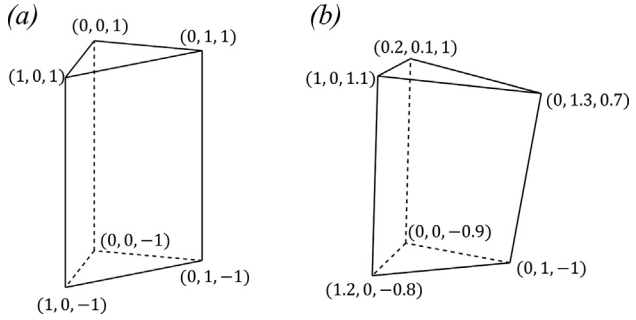

Fig. 5. Prism elements used for the zero energy mode test; the Cartesian coordinates (x, y, z) of nodes are given; units in m; (a) Undistorted prism element; (b) Distorted prism element.

where u_K is the nodal function at node K and ϕ_K^I are partition of unity functions satisfying $\sum_{K=1}^{5} \phi_K^I = 1$. The function ϕ_K^I is defined using the nodal values at the element vertices and at the mid-points of the element sides of the traditional pyramid element with 13 nodes.

$$\phi_K^I = \sum_{i=1}^{13} \hat{h}_i \, \hat{\phi}_{Ki}^I \tag{3}$$

where the $\hat{h}_i$ are the shape functions of the traditional finite element. The values of $\hat{\phi}_{Ki}^I$ are determined using the parameter β, see Appendix A2.

The nodal function u_K can be any suitable function effective for the simulation of the physics of the problem considered (e.g., trigonometric functions [5]), but in this paper a polynomial basis is used as in Ref. [8]. In three-dimensional analyses, we use

$$u_K = a_{K1} + a_{K2}\frac{(x - x_K)}{h} + a_{K3}\frac{(y - y_K)}{h} + a_{K4}\frac{(z - z_K)}{h} + \ldots \tag{4}$$

where the $\boldsymbol{x}_K = (x_K, y_K, z_K)$ are the Cartesian coordinates of node K, the a_{Ki} are unknown variables, and h is the scaling length given by

$$h = \max_{J \in \mathrm{M}} ||\boldsymbol{x}_J - \boldsymbol{x}_K||/2 \tag{5}$$

where M is the set of the element vertices contained in the polyhedral element pertaining to node K [8].

The interpolation Eq. (1) can be expressed as

$$u(\boldsymbol{x}) = \sum_{I=1}^{5} h_I \psi_I = \sum_{I=1}^{5} h_I \left(\sum_{K=1}^{5} \phi_K^I \, u_K \right) = \sum_{K=1}^{5} \left(\sum_{I=1}^{5} h_I \, \phi_K^I \right) u_K$$
$$= \sum_{K=1}^{5} \rho_K \, u_K \tag{6}$$

where the partition of unity $\sum_{K=1}^{5} \rho_K = 1$ is satisfied. As for the prior overlapping elements proposed in Ref. [8], algebraic manipulations give

$$\rho_K = \sum_{I=1}^{5} h_I \, \phi_K^I = \sum_{I=1}^{5} h_I \left(\sum_{i=1}^{13} \hat{h}_i \, \hat{\phi}_{Ki}^I \right) = h_K + \beta \sum_J (h_J - h_K) \, \hat{h}_{JK} \tag{7}$$

where J indicates a node (vertex) directly connected to node K by an element edge and $\hat{h}_{JK}$ is the element shape function corresponding to the mid-side point between nodes J and K.

Table 4
Zero energy mode test for the prism overlapping element; the eigenvalues λ_i are given in ascending order; the first, second, and third rows are corresponding to the use of the linear, bilinear, and quadratic basis, respectively; in all cases, we regard the very small values of $\lambda_1, \lambda_2, \ldots$, and λ_6 as zeros.

element	λ_1	λ_2	λ_3	λ_4	λ_5	λ_6	λ_7	λ_8
Undistorted	-4.51×10^{-9}	2.46×10^{-8}	3.24×10^{-8}	9.50×10^{-8}	2.10×10^{-7}	2.84×10^{-7}	2.31×10^{4}	2.58×10^{4}
	-1.92×10^{-7}	-1.82×10^{-7}	-5.12×10^{-8}	-8.28×10^{-9}	3.04×10^{-8}	1.92×10^{-7}	8.66×10^{0}	1.44×10^{1}
	-1.36×10^{-7}	-1.40×10^{-8}	3.17×10^{-8}	5.29×10^{-8}	9.94×10^{-8}	1.98×10^{-7}	4.60×10^{-1}	1.03×10^{0}
Distorted	-4.22×10^{-8}	1.24×10^{-9}	2.66×10^{-8}	5.85×10^{-8}	8.64×10^{-8}	1.72×10^{-7}	2.17×10^{4}	2.69×10^{4}
	-1.09×10^{-7}	-3.26×10^{-8}	4.61×10^{-9}	9.65×10^{-8}	1.66×10^{-7}	1.71×10^{-7}	3.52×10^{1}	3.64×10^{1}
	-6.64×10^{-8}	-4.16×10^{-8}	2.72×10^{-8}	1.08×10^{-7}	1.56×10^{-7}	2.26×10^{-7}	1.10×10^{0}	1.28×10^{0}

The geometry of the element is interpolated using the functions h_I. From the functions h_I of the nodes on the base, we linearly vary the bilinear interpolation functions along the t-direction, see Fig. 1. See Appendix A1 for the interpolation functions.

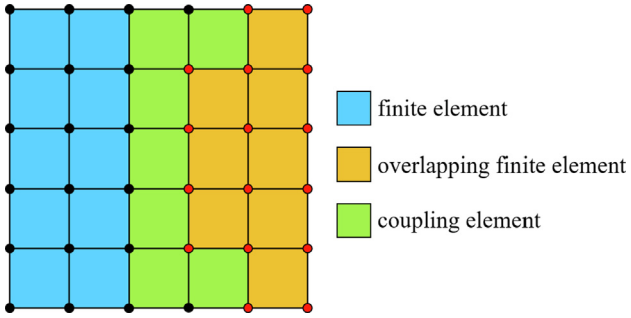

Fig. 6. Description of coupling elements; black and red nodes indicate finite element and overlapping element nodes, respectively; coupling elements are the elements having both finite and overlapping element nodes. (For interpretation of the references to colour in this figure legend, the reader is referred to the web version of this article.)

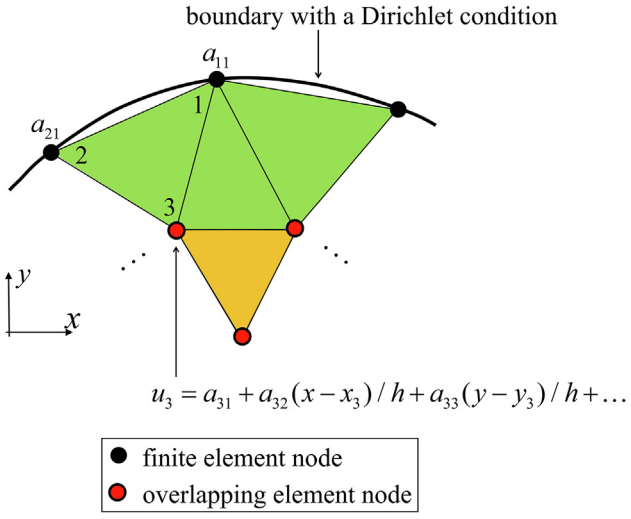

Fig. 7. Placement of finite element nodes on the boundary with a displacement boundary condition; the nodal values at finite element nodes 1 and 2 and the nodal function at overlapping element node 3 are shown.

The pyramid overlapping element is compatible with the brick and the tetrahedral overlapping elements when the same β value is used, see Ref. [8] for the two elements.

Considering the zero energy mode test for the new pyramid element, we calculate the eigenvalues of the stiffness matrix of an unsupported element. An *unsupported* element denotes an element for which all degrees of freedom (dofs) are free. A three-dimensional unsupported element should exhibit only six zero eigenvalues (which correspond to the rigid body modes) if no spurious mode exists [1]. The numerical integration rules suggested in Table 1 and Fig. 2 are used. We consider the undistorted and distorted elements illustrated in Fig. 3. Young's modulus = 2×10^9 Pa, Poisson's ratio = 0.3, and $\beta = 0.03$ are used in the test. As shown in Table 2, the elements pass the zero energy mode test. Note that the numerical round-off error prevents it to obtain exact zero eigenvalues. We also note that the mesh of the pyramid overlapping element passes the patch test when used with the suggested integration rules.

2.2. The prism overlapping finite element

The prism overlapping finite element is formulated as the pyramid overlapping element. A displacement component in the prism overlapping element is interpolated as

$$u(\boldsymbol{x}) = \sum_{I=1}^{6} h_I \psi_I \tag{8}$$

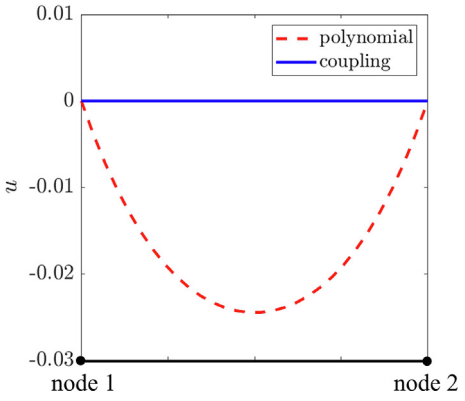

Fig. 9. Distributions of the x-displacement along the straight edge 1–2 in Fig. 8 calculated using the two different methods to impose the boundary condition; the labels "polynomial" and "coupling" represent the use of the appropriate polynomials and the coupling element, respectively.

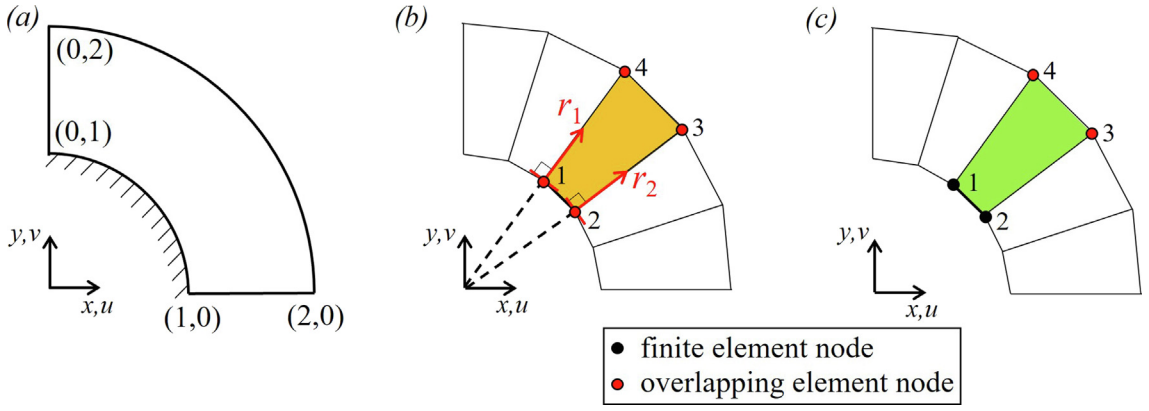

Fig. 8. Comparison of two methods imposing the zero-displacement boundary condition; (a) the analysis domain is shown with the boundary condition; (b) the use of appropriate polynomials; (c) the use of the coupling element.

where the h_I are the shape functions of the 6-node traditional prism finite element and ψ_I is the field of the polyhedral element of node I. The field ψ_I is given as

$$\psi_I = \sum_{K=1}^{6} \phi_K^I \, u_K \tag{9}$$

where the u_K are nodal polynomials and ϕ_K^I satisfy $\sum_{K=1}^{6} \phi_K^I = 1$. We use

$$\phi_K^I = \sum_{i=1}^{15} \hat{h}_i \, \hat{\phi}_{Ki}^I \tag{10}$$

where the $\hat{h}_i$ are the shape functions of the traditional prism finite element with mid-side nodes and $\hat{\phi}_{Ki}^I$ are given using the parameter β, see Appendix A2. We note that the prism element functions also satisfy $u(\boldsymbol{x}) = \sum_{K=1}^{6} \rho_K u_K$ with $\sum_{K=1}^{6} \rho_K = 1$ and

$$\begin{aligned} \rho_K &= \sum_{I=1}^{6} h_I \, \phi_K^I = \sum_{I=1}^{6} h_I \left(\sum_{i=1}^{15} \hat{h}_i \, \hat{\phi}_{Ki}^I \right) \\ &= h_K + \beta \sum_J \left(h_J - h_K \right) \hat{h}_{JK} \end{aligned} \tag{11}$$

where J and $\hat{h}_{JK}$ are defined as in Eq. (7). The prism overlapping element is also compatible with both the brick and tetrahedral overlapping elements [8] provided that the same β value is used.

The geometry of the element is interpolated using the reference element of the 6-node prism finite element, see Fig. 4. The interpolation functions are given in Appendix A1.

As with the other elements, for the new prism element, we also conduct the zero energy mode test. For the numerical integration,

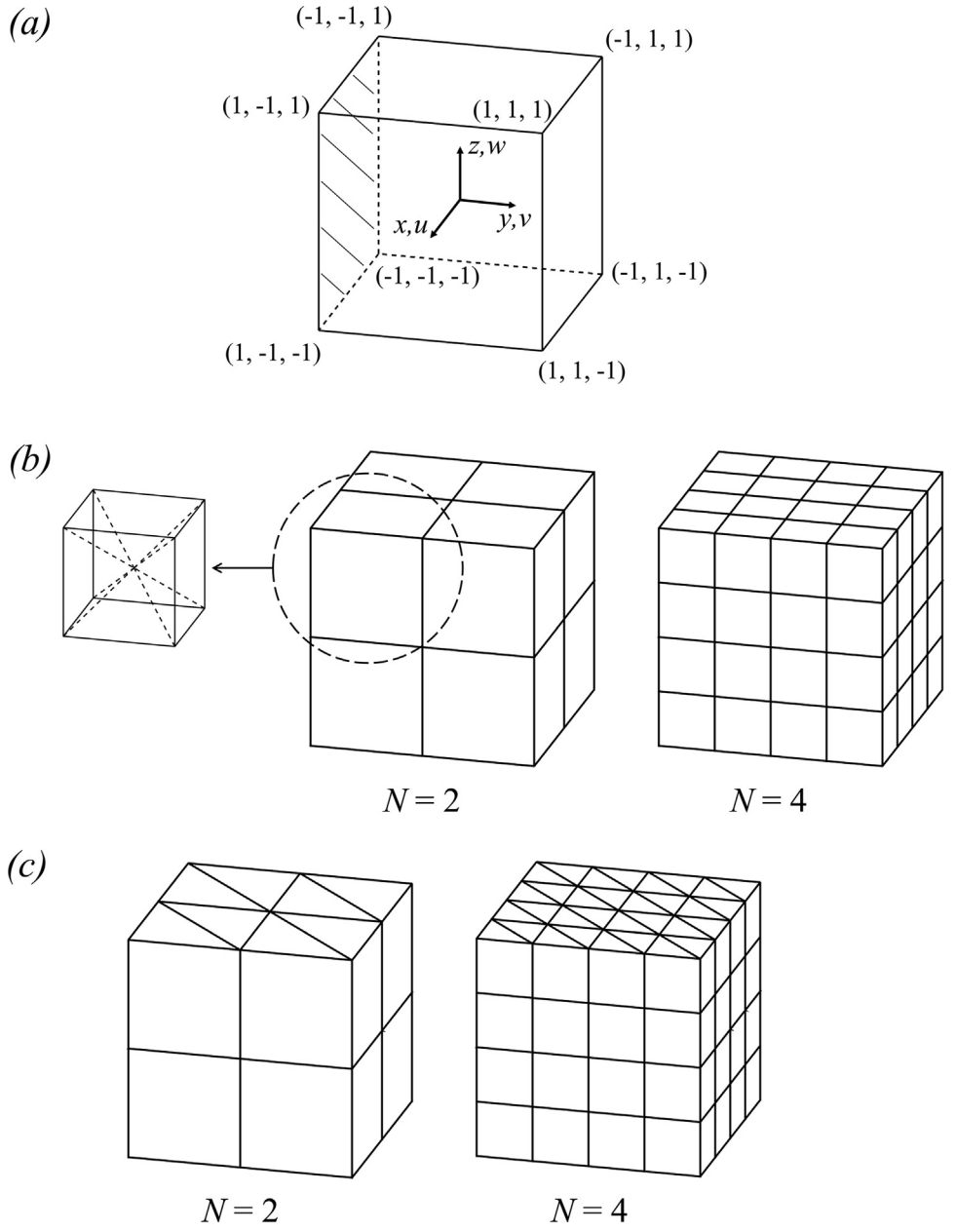

Fig. 10. Adhoc problem; (a) Description of the analysis domain; units in m; the zero-displacement boundary condition is imposed on $y = -1$; Young's modulus = 200 GPa and Poisson's ratio = 0.3 are used; the body force calculated using Eq. (16) is imposed; (b) Meshes using pyramid overlapping elements; as illustrated, a hexahedral domain contains six pyramid elements; (c) Meshes using prism overlapping elements.

we use the rules given in Table 3 over the natural coordinates shown in Fig. 4. The undistorted and distorted elements shown in Fig. 5, also unsupported, are employed in the test. We confirm that the elements pass the test only exhibiting six zero eigenvalues, see Table 4. Again, Young's modulus = 2×10^9 Pa, Poisson's ratio = 0.3, and $\beta = 0.03$ are used in the test.

As shown above, no spurious mode is found in the new pyramid and prism overlapping elements as for the overlapping elements proposed in Ref. [8].

2.3. Coupling element formulation

The coupling element was developed to connect a traditional finite element with an overlapping finite element [3]. Consider the mesh shown in Fig. 6. We see that coupling elements are used for the transition from the finite element mesh to the overlapping element mesh and the coupling elements have both finite element and overlapping element nodes. A displacement component in the coupling element is formulated as

$$
\begin{aligned}
u(\boldsymbol{x}) &= \sum_{I=1}^{N} h_I \psi_I \\
\psi_I &= \begin{cases} \alpha & \text{for } I \in \Lambda_{\text{FE}} \\ \sum_{K \in \Lambda_{\text{OFE}}} \phi_K^I u_K + \sum_{K \in \Lambda_{\text{FE}}} \phi_K^I \alpha & \text{for } I \in \Lambda_{\text{OFE}} \end{cases} \\
\alpha &= \sum_{K=1}^{N} h_K a_{K1}
\end{aligned}
\tag{12}
$$

where Λ_{OFE} and Λ_{FE} are the sets of overlapping and traditional element nodes, respectively, N is the number of nodes (vertices) of the element, and a_{K1} is the traditional nodal value when node K is a finite element node and the constant nodal function value when node K is an overlapping element node.

2.4. Imposition of the Dirichlet boundary conditions

Here we show how coupling elements can be used in the overlapping finite element method to impose the displacement boundary conditions. Consider the analysis domain with a displacement boundary condition shown in Fig. 7. We set the nodes on the

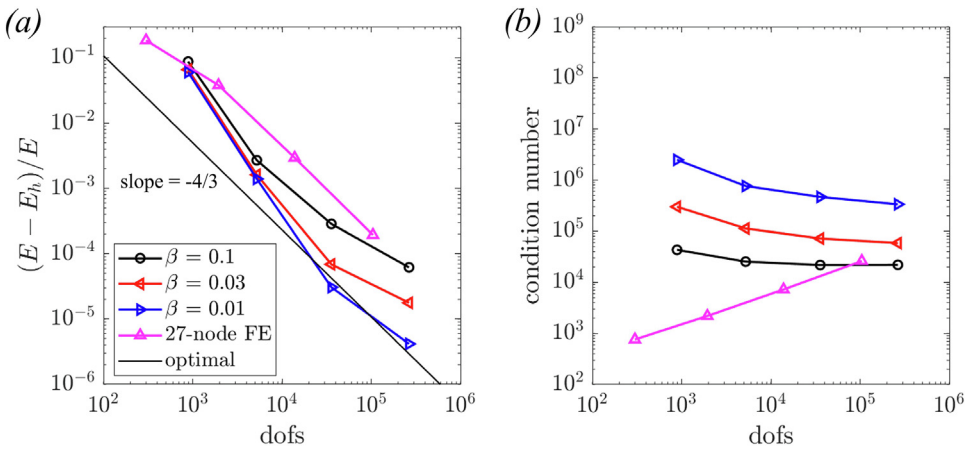

Fig. 11. Adhoc problem solved using the new pyramid overlapping element with the quadratic basis; (a) Convergence of the solutions; (b) Condition number with mesh refinements.

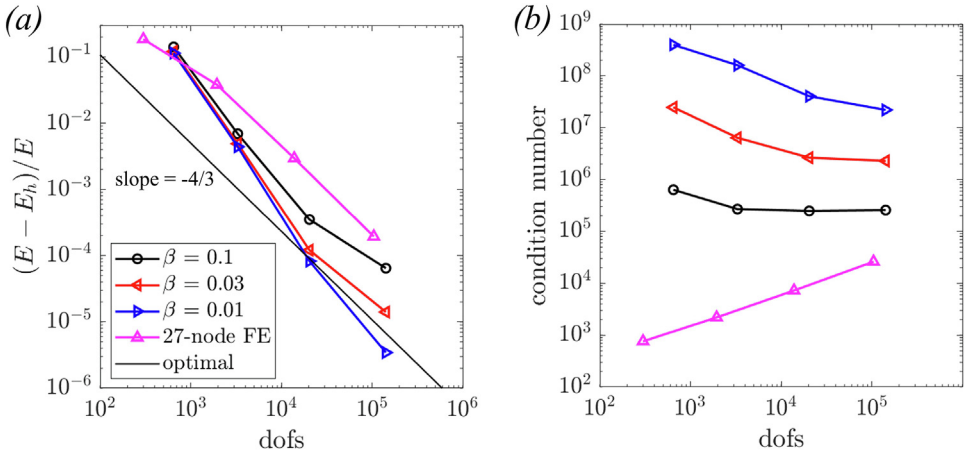

Fig. 12. Adhoc problem solved using the new prism overlapping element with the quadratic basis; (a) Convergence of the solutions; (b) Condition number with mesh refinements.

boundary to be *finite element* nodes and the other nodes to be overlapping element nodes; therefore, the elements along the boundary become coupling elements. We see that along the boundary the displacement interpolation is equal to the finite element interpolation. Considering the x-displacement interpolation along edge 1–2 in Fig. 7, we obtain with the triangular coupling element [8]

$$u|_{1-2} = h_1\psi_1 + h_2\psi_2 + h_3\psi_3 \tag{13}$$

Provided that nodes 1 and 2 are finite element nodes, we use $\psi_1 = \psi_2 = h_1\, a_{11} + h_2\, a_{21} + h_3\, a_{31}$. Given that $h_3 = 0$ on edge 1–2, Eq. (13) becomes

$$u|_{1-2} = (h_1 + h_2)(h_1\, a_{11} + h_2\, a_{21}) = h_1\, a_{11} + h_2\, a_{21} \tag{14}$$

which is the traditional finite element interpolation at the boundary. Hence we can simply impose a displacement boundary condition as usually done in the finite element method. Therefore, all types of the displacement boundary conditions used in the traditional finite element method can directly be imposed in the over-

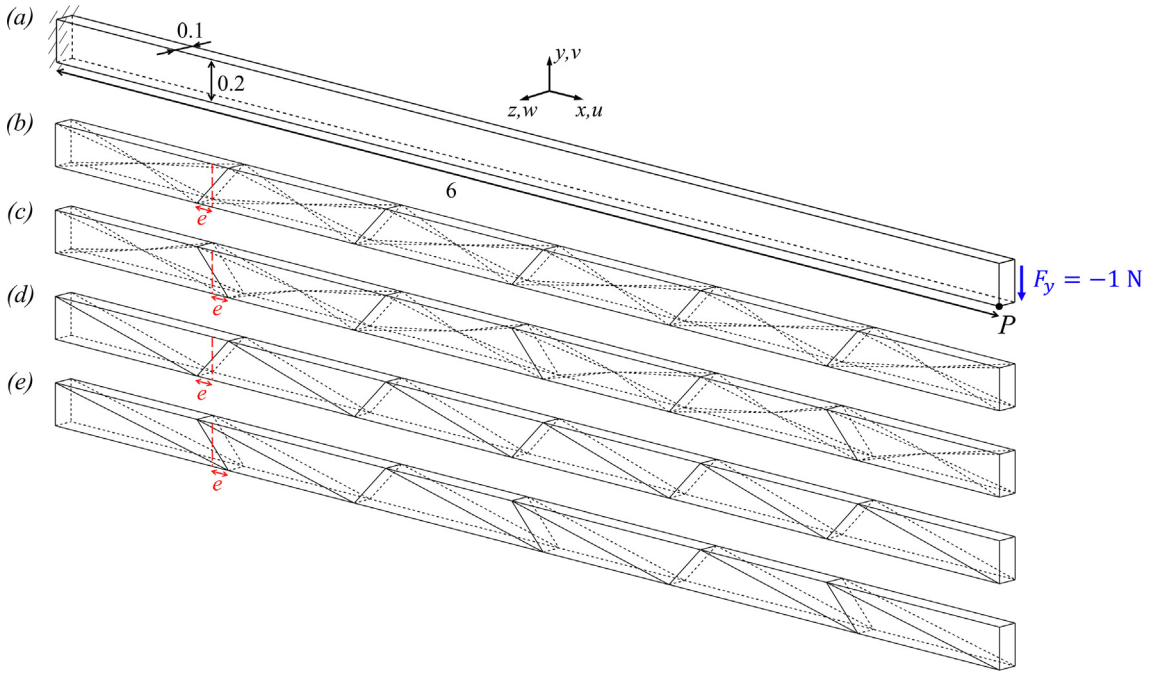

Fig. 13. (a) Description of the slender beam problem; the beam is subject to the shear force $F_y = -1$ N; Young's modulus = 10^7 Pa and Poisson's ratio = 0.3 are used; (b) Parallelogram mesh using pyramid overlapping elements; (c) Trapezoidal mesh using pyramid overlapping elements; (d) Parallelogram mesh using prism overlapping elements; (e) Trapezoidal mesh using prism overlapping elements; the length e represents the extent of distortion; the physical coordinates of an inner node in the meshes of (b) and (c) are given by the mean of the physical coordinates of the respective surrounding eight nodes; lengths in m.

Table 5
Normalized y-direction displacements obtained using the 5-node pyramid and 6-node prism overlapping finite elements; the quadratic basis and $\beta = 0.03$ are used.

5-node pyramid (948 dofs)	$e = 0$ m	0.1	0.2	0.3	0.4
parallelogram	0.9779	0.9717	0.9654	0.9612	0.9570
trapezoidal	0.9779	0.9731	0.9676	0.9638	0.9601
6-node prism (768 dofs)	0	0.1	0.2	0.3	0.4
parallelogram	0.9824	0.9829	0.9835	0.9847	0.9865
trapezoidal	0.9824	0.9798	0.9766	0.9738	0.9725

Table 6
Normalized y-direction displacements obtained using the 5-node pyramid and 6-node prism overlapping finite elements; the quadratic basis and $\beta = 0.01$ are used.

5-node pyramid (948 dofs)	$e = 0$ m	0.1	0.2	0.3	0.4
parallelogram	0.9850	0.9846	0.9841	0.9834	0.9825
trapezoidal	0.9850	0.9846	0.9841	0.9834	0.9826
6-node prism (768 dofs)	0	0.1	0.2	0.3	0.4
parallelogram	0.9864	0.9874	0.9884	0.9895	0.9907
trapezoidal	0.9864	0.9851	0.9836	0.9817	0.9803

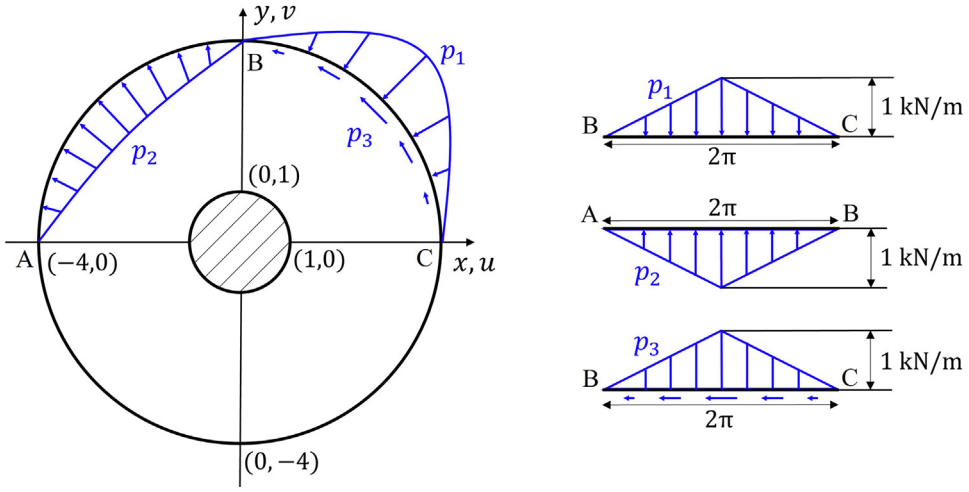

Fig. 14. Description of the shaft problem; the inner surface of the shaft is fixed to the circular rod, and the shown tractions are applied; Young's modulus =200 GPa, Poisson's ratio =0.3, and plane strain conditions are considered; lengths in m.

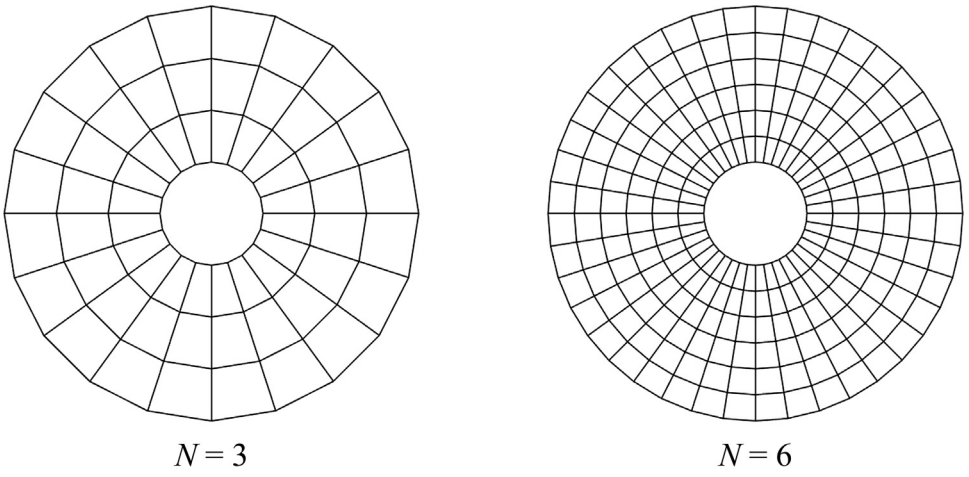

Fig. 15. Meshes used for the shaft problem; N represents the number of element layers along the radial direction; for the convergence test we use N = 3, 6, 12, and 24; the mesh refined uniformly.

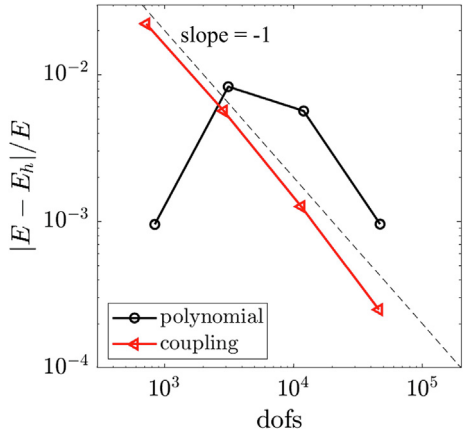

Fig. 16. Convergence of the strain energy obtained using two different schemes to impose the boundary condition; the label "polynomial" represents the scheme that uses appropriate nodal polynomials, and the label "coupling" denotes the use of coupling elements.

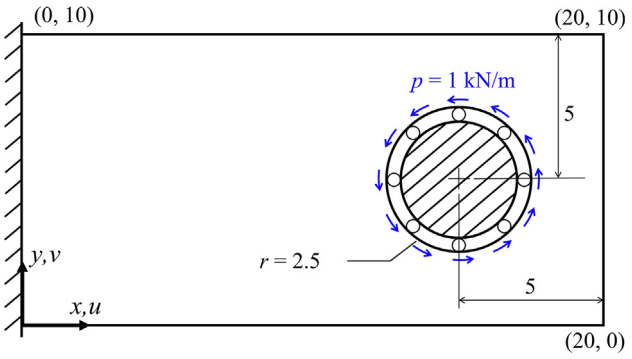

Fig. 17. Description of the plate problem; the plate is subjected to a uniform torsion; the boundary of the hole is on rollers; Young's modulus =200 GPa, Poisson's ratio =0.3, and plane stress conditions are considered; lengths in m.

lapping finite element method using the coupling element. This is not the case with the previously used scheme [8] where we utilize appropriate nodal local coordinates and nodal functions to impose the boundary conditions.

To compare the previous and new schemes, we consider the imposition of the zero-displacement boundary condition on a two-dimensional arc-shaped boundary, see Fig. 8(a). As shown in Fig. 8(b) where the 4-node overlapping element, with overlapping nodes, is used on the boundary [8], the previous scheme introduces nodal local coordinates that are perpendicular to the tangential direction of the boundary. Considering the x-displacement interpolation along edge 1–2 in Fig. 8(b) and the use of the linear basis, we use the appropriate nodal functions $u_1 = a_{12}r_1$, $u_2 = a_{22}r_2$ and obtain the x-displacement of

$$\begin{aligned} u|_{1-2} &= \rho_1 u_1 + \rho_2 u_2 + \rho_3 u_3 + \rho_4 u_4 \\ &= \rho_1 u_1 + \rho_2 u_2 \\ &= \rho_1 a_{12} r_1 + \rho_2 a_{22} r_2 \end{aligned} \tag{15}$$

where we use $\rho_3 = \rho_4 = 0$ along edge 1–2. We notice that Eq. (15) does not give the zero x-displacement at all points on the edge 1–2. For example, Fig. 9 shows the x-displacement field along edge 1–2 when we assume $a_{12} = a_{22} = 1$ with $\beta = 0.1$. We notice the x-displacement is zero only at the boundary nodes when the appropriate polynomials are used whereas the use of the coupling element shown in Fig. 8(c) enables the exact displacement imposition.

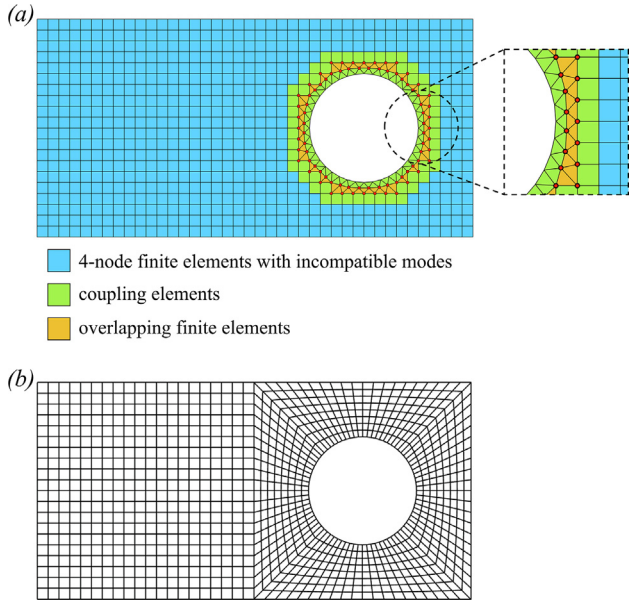

Fig. 18. Meshes used to solve the plate problem; (a) AMORE mesh using the quadratic basis and $\beta = 0.01$ (2,430 dofs); red nodes indicate overlapping element nodes; (b) Traditional mesh using the 4-node finite element with incompatible modes (2,238 dofs). (For interpretation of the references to colour in this figure legend, the reader is referred to the web version of this article.)

Table 7
Numerical results for the plate problem; the reference solutions for strain energy, maximum von Mises stress, maximum x-displacement ($u_{\max}$), and minimum y-displacement ($v_{\min}$) are 3.423×10^{-4} J, 2.158 kPa, 7.719×10^{-5} mm, and -3.627×10^{-5} mm, respectively; all values are the normalized.

mesh	strain energy	maximum von Mises stress	$u_{\max}$	$v_{\min}$
Traditional (2,238 dofs)	0.9972	0.9194	0.9966	0.9984
AMORE (2,430 dofs)	0.9934	0.9594	0.9954	0.9954

3. Illustrative analyses

In this section, we first numerically investigate the convergence rate, conditioning, and distortion sensitivity of each new element. Thereafter, numerical examples using coupling elements to impose the Dirichlet conditions are provided. We also show the use of the new overlapping elements in the AMORE scheme and their effectiveness.

3.1. An adhoc problem

First, we solve a linear static adhoc problem using the new pyramid overlapping element with the quadratic basis. The analysis domain and boundary condition used are shown in Fig. 10(a), see Refs. [8,12]. The domain is subject to a body force, and the body force is calculated using the displacements

$$\begin{aligned} u &= (1-x^2)^2(1-y^2)^2(1-z^2)^2 e^y \cos(x)\sin(y)\cos(z) \\ v &= (1-x^2)^2(1-y^2)^2(1-z^2)^2 e^y \sin(x)\cos(y)\cos(z) \\ w &= (1-x^2)^2(1-y^2)^2(1-z^2)^2 e^y \cos(x)\cos(y)\sin(z) \end{aligned} \tag{16}$$

Therefore Eq. (16) is the exact solution of the problem. The solution convergence and the conditioning of the governing equations are examined with the meshes using $N = 2, 4, 8, 16$ where N is the number of elements per side of the analysis domain, see Fig. 10(b).

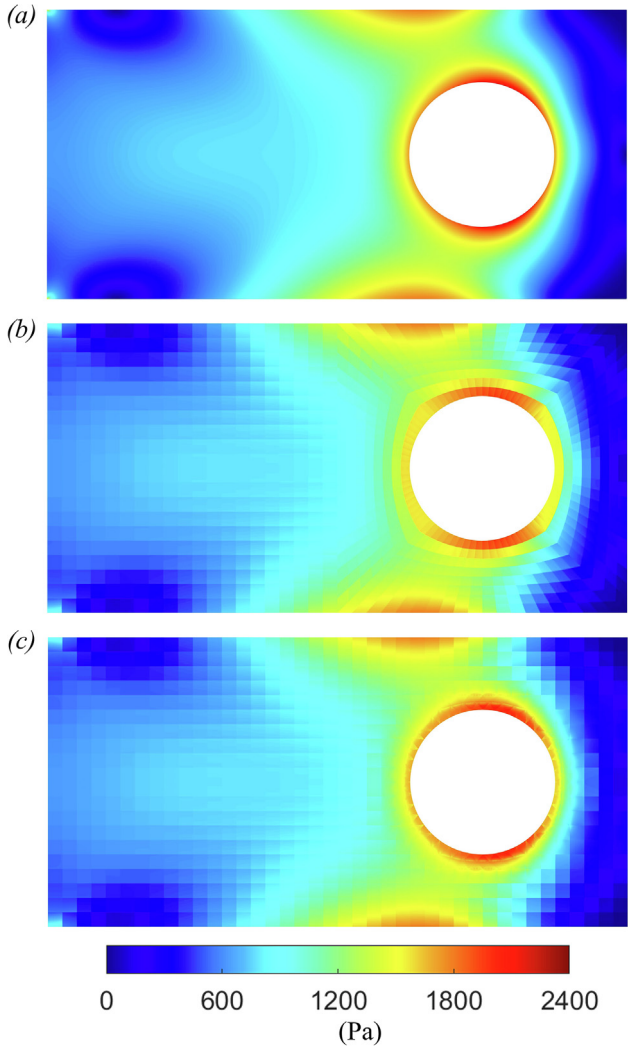

Fig. 19. von Mises stress fields; (a) Reference solution; (b) Solution obtained using the traditional mesh; (c) Solution obtained using the AMORE mesh.

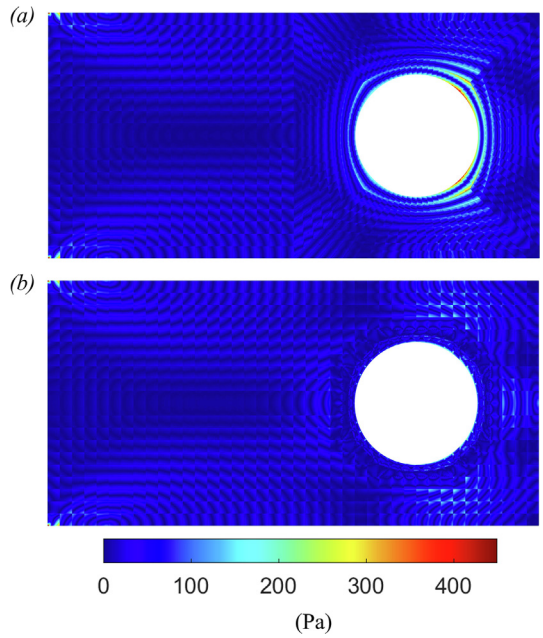

Fig. 20. Absolute error fields of the von Mises stress; (a) Traditional mesh; (b) AMORE mesh.

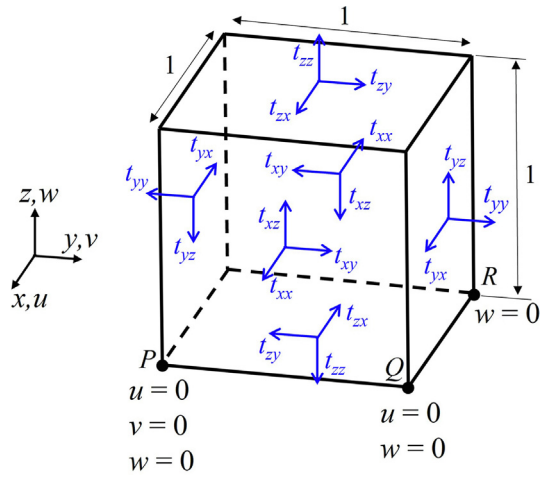

Fig. 21. Description of the patch test; Young's modulus = 100 Pa and Poisson's ratio = 0.3 are considered; the analysis domain is subject to the tractions of $t_{xx} = t_{yy} = t_{zz} = 1$ Pa, $t_{xy} = t_{yx} = 1$ Pa, $t_{yz} = t_{zy} = 2$ Pa, and $t_{zx} = t_{xz} = 3$ Pa; the minimum displacement boundary conditions are imposed at nodes *P*, *Q*, and *R* in order to remove rigid body modes; lengths in m.

The zero-displacement boundary condition is imposed using appropriate nodal polynomials on the boundary [8] (i.e., using the "previous" scheme referred in Section 2.4). We note that for this problem the previous scheme is giving more accurate results because overlapping nodes with polynomials are used on the boundary and the scheme imposes the boundary condition exactly. In Fig. 11, the strain energy error and the condition number of the stiffness matrix are given with respect to the number of degrees of freedom (dofs) used. We note that E and E_h are the reference and predicted strain energy, respectively. The problem is also solved using the 27-node brick finite element for comparison. The results using the new pyramid element show convergence rates well agreeing with theory [7], and the condition numbers are reasonable and tend to slightly decrease with mesh refinements. A smaller β gives a faster convergence but an increased condition number. We described this trend also when using our earlier published enhanced overlapping elements [8].

The prism overlapping element with the quadratic basis is also tested in the same way using the meshes shown in Fig. 10(c). Fig. 12 illustrates that the use of new prism element results also into good convergence rates. The resulting condition numbers are larger than those of the new pyramid element for about the same number of dofs but are still reasonable. The trends regarding the use of β are like those found when using the new pyramid element.

3.2. A slender beam problem

The distortion sensitivities of the new elements are studied using the slender beam problem shown in Fig. 13(a), see Refs. [8,13]. We solve for the y-displacement at point P and consider the parallelogram and trapezoidal distortions described in Fig. 13. The reference solution is −0.1081 m. The pyramid and prism overlapping elements using the quadratic basis are used with $\beta = 0.03$ and 0.01. As in the previous adhoc problem, the boundary condition is imposed using appropriate nodal polynomials on the boundary. Both new elements provide quite accurate solutions regardless of "e" which represents the degree of the element distortion, see Table 5 and Table 6. We see that the use of the smaller β provides more accurate displacement predictions which are also less sensitive to the mesh distortions.

3.3. A shaft problem with the zero-displacement boundary condition

We now consider the use of coupling elements for imposing the zero-displacement boundary condition on a curved boundary. We solve the problem illustrated in Fig. 14 (see Ref. [4]) and employ the 4-node quadrilateral overlapping element [8] using the quadratic basis with $\beta = 0.01$. The zero-displacement boundary condition is imposed by setting the nodes on the boundary to be finite element nodes; therefore, the elements on the boundary are cou-

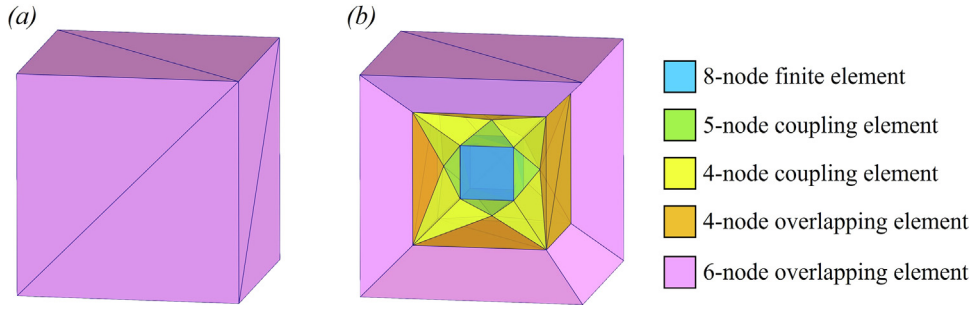

Fig. 22. (a) AMORE mesh used for the patch test; (b) AMORE mesh partially shown.

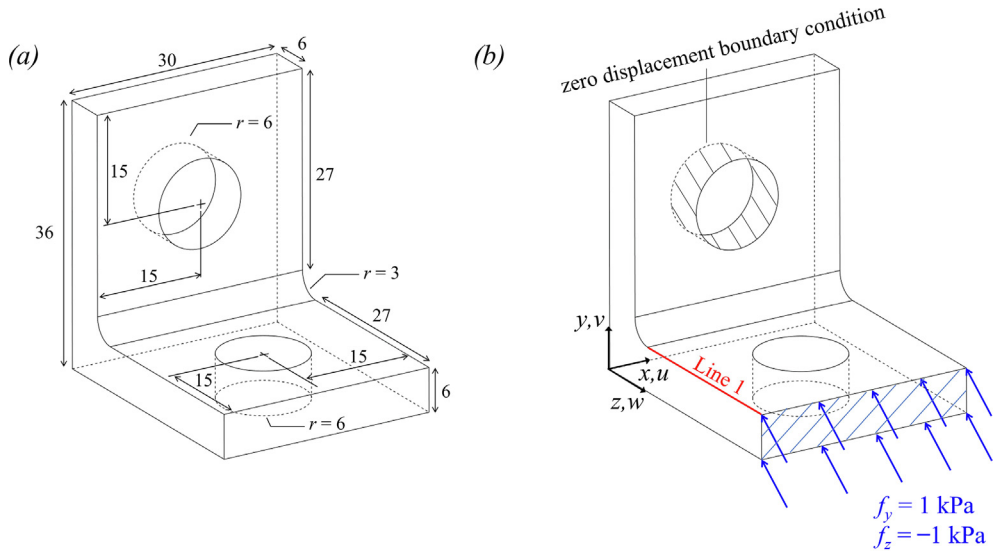

Fig. 23. Three dimensional bracket problem solved using the AMORE scheme; Young's modulus = 200 GPa and Poisson's ratio = 0.3 are considered; (a) Dimensions of the bracket; lengths in mm; (b) the fixed boundary condition is imposed on the cylindrical surface of the indicated hole; the surface traction of $f_y = 1$ kPa and $f_z = -1$ kPa is applied on the surface marked with blue lines. (For interpretation of the references to colour in this figure legend, the reader is referred to the web version of this article.)

pling elements. We use the meshes described in Fig. 15. For comparison, we also impose the boundary condition using appropriate nodal polynomials on the boundary [8]. We saw in Section 2.4 that the use of appropriate polynomials cannot exactly impose the zero-displacement boundary condition on curved boundaries. The results for the problem considered now are given in Fig. 16, and compared to the results obtained using a fine mesh of 9-node finite elements (491,520 dofs). We see that the use of appropriate polynomials does not lead to monotonic convergence unlike using the coupling element on the boundary. Although the quadratic basis is employed, the convergence rate reached using the coupling element is about -1 because the coupling element is only complete up to degree 1.

3.4. A plate problem with a roller boundary condition

Next we consider the use of coupling elements to impose a roller boundary condition. The plate problem shown in Fig. 17 is solved using AMORE and traditional meshes, as described in Fig. 18. The problem considered here is adapted from the problem in Ref. [7]. In the AMORE mesh, the nodes on the boundary with the roller boundary condition are finite element nodes. The overlapping elements presented in Ref. [8] are used with the quadratic basis and $\beta = 0.01$, and the incompatible mode element is employed for the traditional elements [1]. A very fine mesh of the 9-node element (347,518 dofs) is used to obtain the reference solution. As shown in Table 7, both the AMORE and traditional meshes offer reasonable predictions for the strain energy and displacements. However, the AMORE mesh provides a more accurate von Mises stress prediction. We also see from Fig. 19 and Fig. 20 that the AMORE mesh offers a more accurate stress prediction compared with the traditional mesh. Note that we use similar numbers of dofs for the meshes.

3.5. A patch test for an AMORE mesh in 3D

Here, we perform a patch test using an AMORE mesh. The problem described in Fig. 21 is solved using the mesh shown in Fig. 22. An 8-node finite element is located in the middle of the mesh, and the pyramid and tetrahedral coupling elements are used to link the finite element with the outer layers of overlapping finite elements. The 4-node tetrahedral elements are formulated as in Ref. [8][1]. The linear basis and $\beta = 0.03$ are used. The AMORE mesh passes the patch test, exactly reproducing the constant stress state, and also when incompatible modes are added to the 8-node finite element.

3.6. A bracket problem solved using the AMORE scheme

Finally, we solve the bracket problem shown in Fig. 23 using the AMORE scheme. We use the AMORE mesh shown in Fig. 24 where the new elements are utilized to discretize the regions near curved boundaries and the elements presented in Ref. [8] are used. The linear basis and $\beta = 0.01$ are employed in the mesh. Note that the prism coupling elements in the mesh are for imposing the zero-displacement boundary condition and the pyramid coupling elements merge the mesh of incompatible mode elements and the mesh of tetrahedral overlapping elements. For comparison, the use of the traditional mesh shown in Fig. 24 is also considered.

The AMORE and traditional meshes give the normalized strain energy of 0.98 and 0.97, respectively. The reference strain energy is 2.885×10^{-9} J which is obtained using a fine mesh of 10-node tetrahedral finite elements (829,215 dofs). The y-direction displacement and von Mises stress along Line 1 (see Fig. 23(b)) are computed. As shown in Fig. 25, both meshes provide reasonable displacement predictions while the AMORE mesh more accurately captures the sudden change in stress gradient. We further examine the von Mises stress distribution on the bracket surfaces, see Fig. 26. We see that the AMORE mesh gives a better stress prediction.

4. Concluding remarks

We proposed two new overlapping finite elements: a pyramid element and a prism element. The elements have been formulated

[1] We use the numerical 11-point integration scheme given in Ref. [8] for the tetrahedral overlapping element with the linear basis but need to note that the correct eigenvalues of the free element (not given here) for the linear and bilinear bases are slightly different from those given in Ref. [8]. The important conclusions, however, that the elements contain no spurious modes still hold.

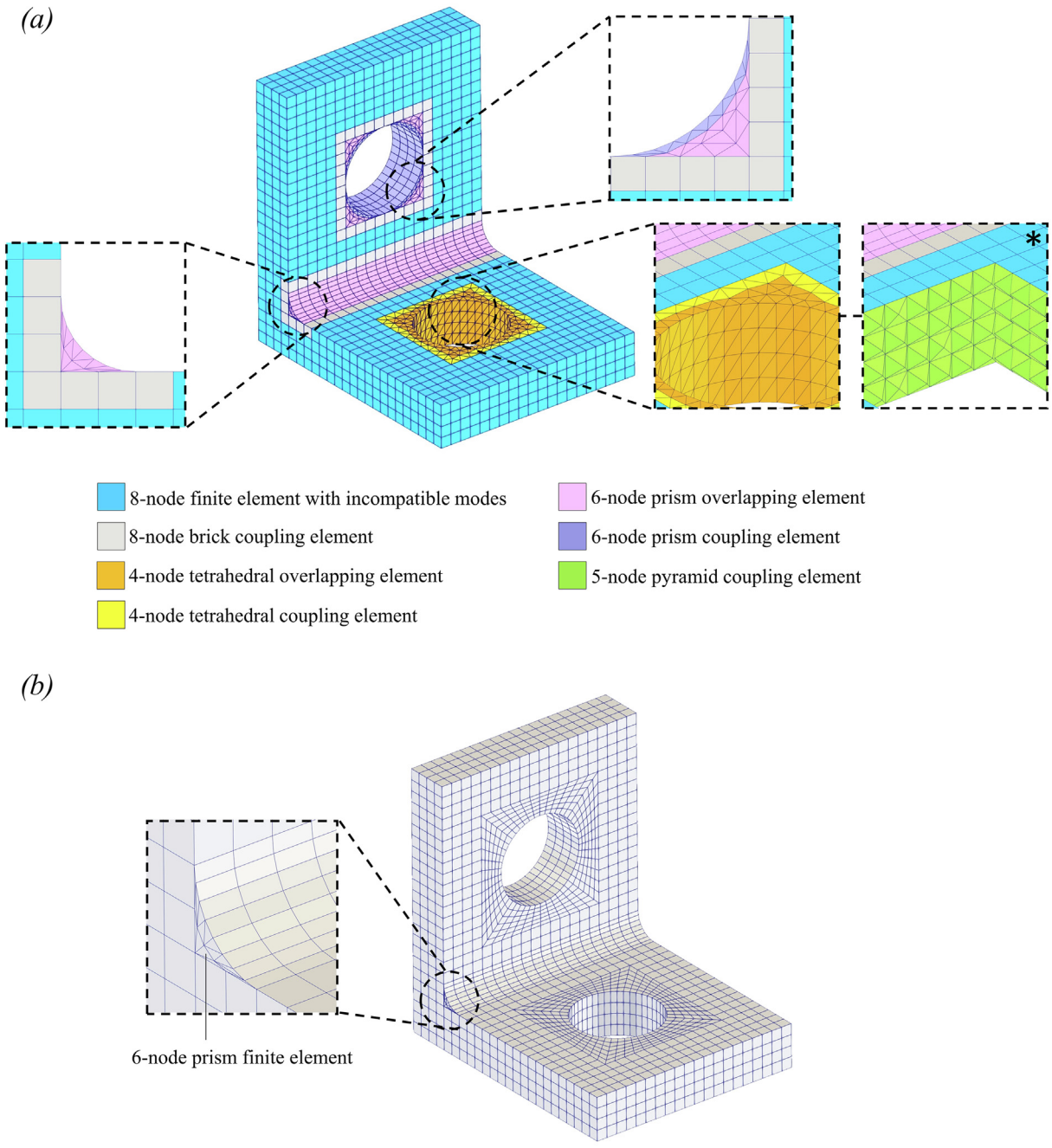

Fig. 24. Meshes used to solve the three dimensional bracket problem; (a) AMORE mesh using the linear basis and $\beta = 0.01$ (26,370 dofs); the pyramid coupling elements used in the mesh are shown in the zoomed image with asterisk; (b) Traditional mesh using the incompatible 8-node finite element and the 6-node prism finite element (19,095 dofs); the fillet of the bracket is discretized using the 6-node prism finite element.

using the theory given in Ref. [8] and are valuable in their use of general meshing of complex geometries.

We have studied the properties of the elements regarding stability and convergence, the condition numbers of solutions, and their insensitivity to element distortions. We also have given the results of illustrative solutions, including the use of the AMORE solution scheme. In addition, we revisited how to best impose displacement boundary conditions when overlapping finite elements are used and obtained new insights.

Based on our experiences, the use of overlapping finite elements shows significant advantages over the use of traditional finite elements, but further research is required for their general applications. We considered only linear static analyses and wave propagation solutions [5]. In addition, other dynamic solutions should be considered, and the use and further development of overlapping finite elements should be pursued for the general nonlinear analysis of structures and solids, heat transfer and multiphysics problem. Finally, also effective meshing schemes for the specific use of the AMORE procedure are needed, and the pyramid and prism elements presented in this paper should be of particular value in such schemes.

Declaration of Competing Interest

The authors declare that they have no known competing financial interests or personal relationships that could have appeared to influence the work reported in this paper.

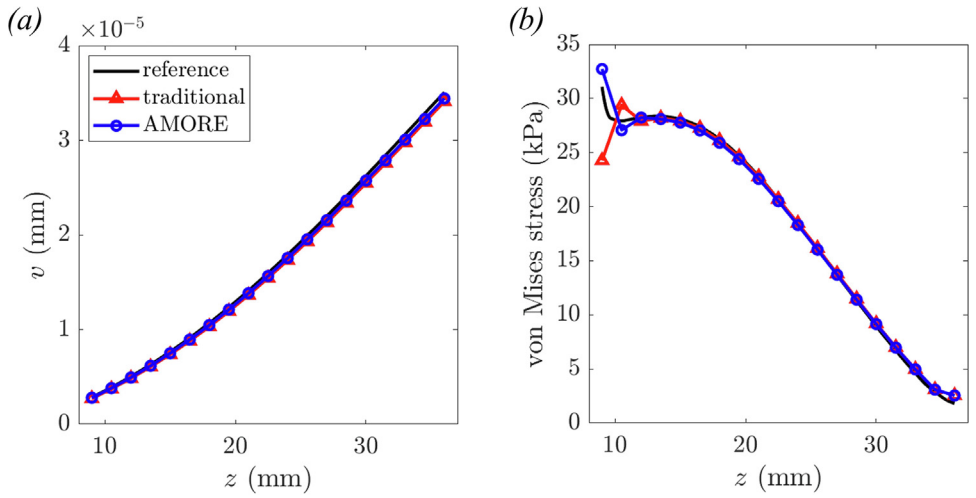

Fig. 25. Numerical predictions along Line 1; (a) *y*-direction displacement; (b) von Mises stress obtained using the averaged nodal stresses.

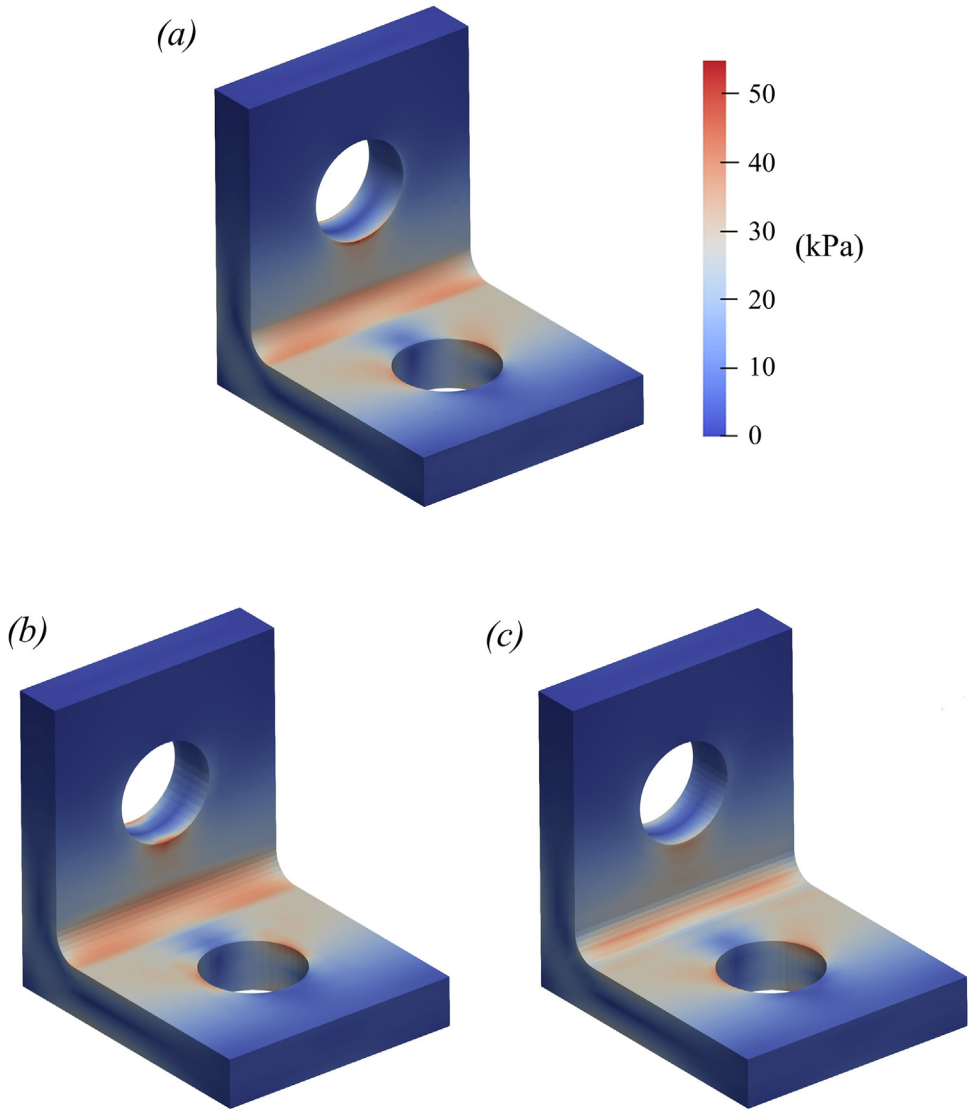

Fig. 26. von Mises stress distributions; all solutions are visualized interpolating the von Mises stress obtained using the averaged nodal stresses; (a) Reference solution; (b) Solution calculated using the AMORE mesh; (c) Solution calculated using the traditional mesh.

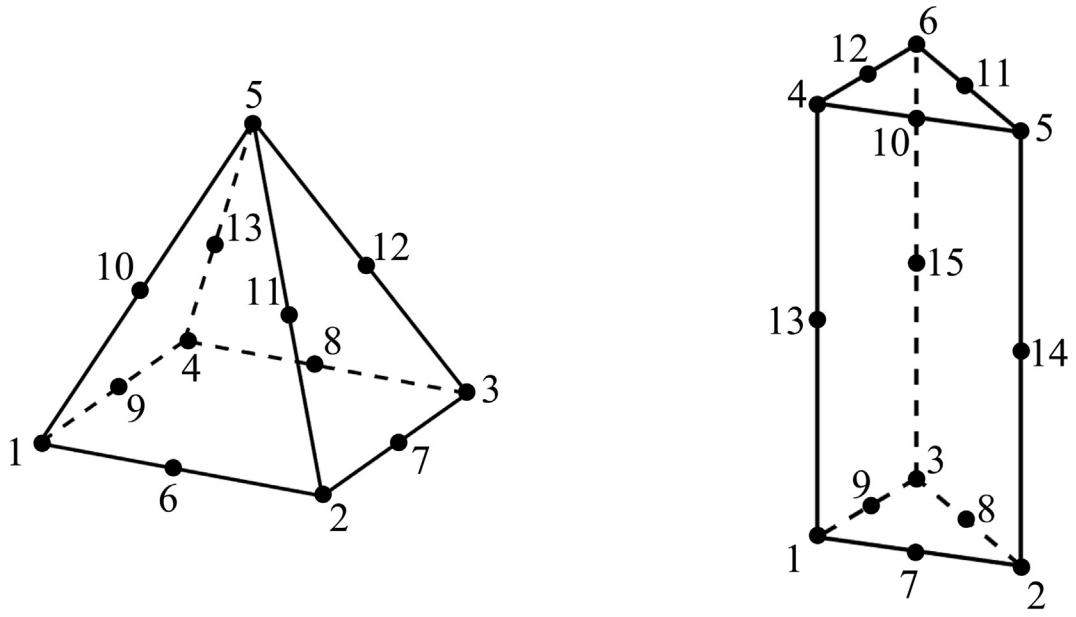

Fig. A1. Node numbering for the new pyramid and prism overlapping elements; we include the nodes only used for the interpolation of ϕ_K^l; the actual physical nodes are 1 to 5 for the pyramid element and 1 to 6 for the prism element.

Table A1
Nodal values for the interpolation of ϕ_K^l of the 5-node pyramid overlapping element.

Nodes	$i=1$	2	3	4	5	6	7	8	9	10	11	12	13
$\hat{\phi}^1_{1i}$	1					*A*			*A*	*A*			
$\hat{\phi}^1_{2i}$		1				*B*	0.5				0.5		
$\hat{\phi}^1_{3i}$			1				0.5	0.5				0.5	
$\hat{\phi}^1_{4i}$				1				0.5	*B*				0.5
$\hat{\phi}^1_{5i}$					1					*B*	0.5	0.5	0.5
$\hat{\phi}^2_{1i}$	1					*B*			0.5	0.5			
$\hat{\phi}^2_{2i}$		1				*A*	*A*				*A*		
$\hat{\phi}^2_{3i}$			1				*B*	0.5				0.5	
$\hat{\phi}^2_{4i}$				1				0.5	0.5				0.5
$\hat{\phi}^2_{5i}$					1					0.5	*B*	0.5	0.5
$\hat{\phi}^3_{1i}$	1					0.5			0.5	0.5			
$\hat{\phi}^3_{2i}$		1				0.5	*B*				0.5		
$\hat{\phi}^3_{3i}$			1				*A*	*A*				*A*	
$\hat{\phi}^3_{4i}$				1				*B*	0.5				0.5
$\hat{\phi}^3_{5i}$					1					0.5	0.5	*B*	0.5
$\hat{\phi}^4_{1i}$	1					0.5			*B*	0.5			
$\hat{\phi}^4_{2i}$		1				0.5	0.5				0.5		
$\hat{\phi}^4_{3i}$			1				0.5	*B*				0.5	
$\hat{\phi}^4_{4i}$				1				*A*	*A*				*A*
$\hat{\phi}^4_{5i}$					1					0.5	0.5	0.5	*B*
$\hat{\phi}^5_{1i}$	1					0.5			0.5	*B*			
$\hat{\phi}^5_{2i}$		1				0.5	0.5				*B*		
$\hat{\phi}^5_{3i}$			1				0.5	0.5				*B*	
$\hat{\phi}^5_{4i}$				1				0.5	0.5				*B*
$\hat{\phi}^5_{5i}$					1					*A*	*A*	*A*	*A*

Appendix A1. Finite element shape functions used for pyramid and prism overlapping elements.

Here we present the finite element shape functions used for the formulations of the pyramid and prism overlapping elements. The node numbering is shown in Fig. A1. Considering the new pyramid overlapping element, we use for the 5-node element:

$$\begin{aligned} h_1 &= \tfrac{1}{8}(1-r)(1-s)(1-t) \\ h_2 &= \tfrac{1}{8}(1+r)(1-s)(1-t) \\ h_3 &= \tfrac{1}{8}(1+r)(1+s)(1-t) \\ h_4 &= \tfrac{1}{8}(1-r)(1+s)(1-t) \\ h_5 &= \tfrac{t+1}{2} \end{aligned} \tag{A.1}$$

and for the interpolation of ϕ_K^I

$$\begin{aligned} \hat{h}_1 &= -(1-r)(1-s)(1-t)(4+3r+3s+2rs+2t+rt+st+2rst)/16 \\ \hat{h}_2 &= -(1+r)(1-s)(1-t)(4-3r+3s-2rs+2t-rt+st-2rst)/16 \\ \hat{h}_3 &= -(1+r)(1+s)(1-t)(4-3r-3s+2rs+2t-rt-st+2rst)/16 \\ \hat{h}_4 &= -(1-r)(1+s)(1-t)(4+3r-3s-2rs+2t+rt-st-2rst)/16 \\ \hat{h}_5 &= t(t+1)/2 \\ \hat{h}_6 &= (1-r^2)(1-s)(1-t)(2+s+st)/8 \\ \hat{h}_7 &= (1-s^2)(1+r)(1-t)(2-r-rt)/8 \\ \hat{h}_8 &= (1-r^2)(1+s)(1-t)(2-s-st)/8 \\ \hat{h}_9 &= (1-s^2)(1-r)(1-t)(2+r+rt)/8 \\ \hat{h}_{10} &= (1-t^2)(1-s)(1-r)/4 \\ \hat{h}_{11} &= (1-t^2)(1-s)(1+r)/4 \\ \hat{h}_{12} &= (1-t^2)(1+s)(1+r)/4 \\ \hat{h}_{13} &= (1-t^2)(1+s)(1-r)/4 \end{aligned} \tag{A.2}$$

Table A2
Nodal values for the interpolation of ϕ_K^I of the 6-node prism overlapping element.

Nodes	$i=1$	2	3	4	5	6	7	8	9	10	11	12	13	14	15
$\hat{\phi}^1_{1i}$	1						*A*		*A*				*A*		
$\hat{\phi}^1_{2i}$		1					*B*	0.5						0.5	
$\hat{\phi}^1_{3i}$			1					0.5	*B*						0.5
$\hat{\phi}^1_{4i}$				1						0.5		0.5	*B*		
$\hat{\phi}^1_{5i}$					1					0.5	0.5			0.5	
$\hat{\phi}^1_{6i}$						1					0.5	0.5			0.5
$\hat{\phi}^2_{1i}$	1						*B*		0.5				0.5		
$\hat{\phi}^2_{2i}$		1					*A*	*A*						*A*	
$\hat{\phi}^2_{3i}$			1					*B*	0.5						0.5
$\hat{\phi}^2_{4i}$				1						0.5		0.5	0.5		
$\hat{\phi}^2_{5i}$					1					0.5	0.5			*B*	
$\hat{\phi}^2_{6i}$						1					0.5	0.5			0.5
$\hat{\phi}^3_{1i}$	1						0.5		*B*				0.5		
$\hat{\phi}^3_{2i}$		1					0.5	*B*						0.5	
$\hat{\phi}^3_{3i}$			1					*A*	*A*						*A*
$\hat{\phi}^3_{4i}$				1						0.5		0.5	0.5		
$\hat{\phi}^3_{5i}$					1					0.5	0.5			0.5	
$\hat{\phi}^3_{6i}$						1					0.5	0.5			*B*
$\hat{\phi}^4_{1i}$	1						0.5		0.5				*B*		
$\hat{\phi}^4_{2i}$		1					0.5	0.5						0.5	
$\hat{\phi}^4_{3i}$			1					0.5	0.5						0.5
$\hat{\phi}^4_{4i}$				1						*A*		*A*	*A*		
$\hat{\phi}^4_{5i}$					1					*B*	0.5			0.5	
$\hat{\phi}^4_{6i}$						1					0.5	*B*			0.5
$\hat{\phi}^5_{1i}$	1						0.5		0.5				0.5		
$\hat{\phi}^5_{2i}$		1					0.5	0.5						*B*	
$\hat{\phi}^5_{3i}$			1					0.5	0.5						0.5
$\hat{\phi}^5_{4i}$				1						*B*		0.5	0.5		
$\hat{\phi}^5_{5i}$					1					*A*	*A*			*A*	
$\hat{\phi}^5_{6i}$						1					*B*	0.5			0.5
$\hat{\phi}^6_{1i}$	1						0.5		0.5				0.5		
$\hat{\phi}^6_{2i}$		1					0.5	0.5						0.5	
$\hat{\phi}^6_{3i}$			1					0.5	0.5						*B*
$\hat{\phi}^6_{4i}$				1						0.5		*B*	0.5		
$\hat{\phi}^6_{5i}$					1					0.5	*B*			0.5	
$\hat{\phi}^6_{6i}$						1					*A*	*A*			*A*

For the 6-node prism overlapping element, we employ

$$\begin{aligned} h_1 &= \tfrac{1}{2}(1-r-s)(1-t),\ \ h_2 = \tfrac{1}{2}r(1-t) \\ h_3 &= \tfrac{1}{2}s(1-t),\ \ h_4 = \tfrac{1}{2}(1-r-s)(1+t) \\ h_5 &= \tfrac{1}{2}r(1+t),\ \ h_6 = \tfrac{1}{2}s(1+t) \end{aligned} \tag{A.3}$$

and for the interpolation of ϕ_K^I

$$\begin{aligned} \hat{h}_1 &= -(1-r-s)(1-t)\left(r+s+\tfrac{t}{2}\right),\ \ \hat{h}_2 = r(1-t)\left(r-\tfrac{t}{2}-1\right) \\ \hat{h}_3 &= s(1-t)\left(s-\tfrac{t}{2}-1\right),\ \ \hat{h}_4 = -(1-r-s)(1+t)\left(r+s-\tfrac{t}{2}\right) \\ \hat{h}_5 &= r(1+t)\left(r+\tfrac{t}{2}-1\right),\ \ \hat{h}_6 = s(1+t)\left(s+\tfrac{t}{2}-1\right) \\ \hat{h}_7 &= 2r(1-r-s)(1-t),\ \ \hat{h}_8 = 2rs(1-t) \\ \hat{h}_9 &= 2s(1-r-s)(1-t),\ \ \hat{h}_{10} = 2r(1-r-s)(1+t) \\ \hat{h}_{11} &= 2rs(1+t),\ \ \hat{h}_{12} = 2s(1-r-s)(1+t) \\ \hat{h}_{13} &= (1-r-s)\left(1-t^2\right),\ \ \hat{h}_{14} = r\left(1-t^2\right),\ \ \hat{h}_{15} = s\left(1-t^2\right) \end{aligned} \tag{A.4}$$

Appendix A2. Values of $\hat{\phi}_{Ki}^I$ for interpolating ϕ_K^I

The nodal values $\hat{\phi}_{Ki}^I$ to interpolate ϕ_K^I are given in Tables A1 and A2. In the tables, $A = 0.5 - \beta$, $B = 0.5 + \beta$, and a blank cell denotes the value of zero. See Fig. A1 for the node numbering.

References

[1] Bathe KJ. Finite element procedures. Prentice Hall; 1996. 2nd ed. KJ Bathe, Watertown, MA; 2014, and Higher Education Press, Beijing; 2016.

[2] Lee NS, Bathe KJ. Effects of element distortions on the performance of isoparametric elements. Int J Numer Methods Eng 1993;36:3553–76.

[3] Bathe KJ. The AMORE paradigm for finite element analysis. Adv Eng Softw 2019;130:1–13.

[4] Zhang L, Kim K-T, Bathe KJ. The new paradigm of finite element solutions with overlapping elements in CAD – computational efficiency of the procedure. Comput Struct 2018;199:1–17.

[5] Kim K-T, Zhang L, Bathe KJ. Transient implicit wave propagation dynamics with overlapping finite elements. Comput Struct 2018;199:18–33.

[6] Huang J, Bathe KJ. Quadrilateral overlapping elements and their use in the AMORE paradigm. Comput Struct 2019;222:25–35.

[7] Huang J, Bathe KJ. On the convergence of overlapping elements and overlapping meshes. Comput Struct 2021;244:106429.

[8] Lee S, Bathe KJ. An enhancement of overlapping finite elements. Comput Struct 2022;260:106704.

[9] Strouboulis T, Babuška I, Copps K. The design and analysis of the generalized finite element method. Comput Methods Appl Mech Eng 2000;181:43–69.

[10] Tian R, Yagawa G, Terasaka H. Linear dependence problems of partition of unity-based generalized FEMs. Comput Methods Appl Mech Eng 2006;195:4768–82.

[11] Cowper GR. Gaussian quadrature formulas for triangles. Int J Numer Methods Eng 1973;7:405–8.

[12] Kim S, Lee PS. New enriched 3D solid finite elements: 8-node hexahedral, 6-node prismatic, and 5-node pyramidal elements. Comput Struct 2019;216:40–63.

[13] MacNeal RH. A theorem regarding the locking of tapered four-noded membrane elements. Int J Numer Methods Eng 1987;24:1793–9.